Aerospace Science and Technology 41 (2015) 175–188

Contents lists available at ScienceDirect

Aerospace Science and Technology

www.elsevier.com/locate/aescte

High maneuverability projectile flight using low cost components

Frank Fresconi [a], Ilmars Celmins [a], Sidra Silton [a], Mark Costello [b]

[a] U.S. Army Research Laboratory, Aberdeen Proving Ground, MD 21015, United States
[b] Georgia Institute of Technology, Atlanta, GA 30332, United States

ARTICLE INFO

Article history:
Received 26 March 2014
Received in revised form 23 September 2014
Accepted 1 December 2014
Available online 29 December 2014

Keywords:
Projectile
Guided flight
High maneuverability
Low cost

ABSTRACT

This paper examines the problem of enhancing maneuverability of gun-launched munitions utilizing low cost technologies. Two ideas are proposed for reducing cost: (1) designing algorithms that reduce the sensor or actuator burden, and (2) performing high fidelity modeling and simulation of the entire system with realistic data input. The fundamental theory underpinning guided projectile flight systems, including nonlinear equations of motion for projectile flight, aerodynamic modeling, actuator dynamics, and measurement modeling, is outlined. Manipulation of these nonlinear models into linear system models enables airframe stability investigation and flight control design. A basic framework for low cost guidance, navigation, and control (GNC) of high maneuverability projectiles is formulated. Theory was implemented in simulation and exercised for a guided projectile system. Results support the hypothesis that algorithms can compensate for poor actuator performance and identified critical trade study parameters. Monte Carlo analysis indicated that the cost associated with measurements of a threshold accuracy rather than actuation technologies prescribes guided system performance.

Published by Elsevier Masson SAS.

1. Introduction

The acquisition opportunities for new weapons systems are increasingly limited due to budget restrictions. This environment requires a major shift in defense research toward low cost technologies. In the past, the typical research progression yielded new weapons often characterized as more complex and of higher cost. A more appropriate research emphasis is cost-effective technologies.

The focus of this study is performance improvement of guided projectiles using low cost components. Precision munitions have enjoyed some development in recent years. Feedback measurements from a laser designator have been used in guided projectiles [12,2]. GPS navigation has been utilized more recently for precision munitions [8,11,5,6]. These past efforts have all focused on indirect fire weapons mainly against stationary targets. The airframes either featured low inherent maneuverability or the nature of the feedback measurements did not permit intercepting moving targets.

This study extends past work in guided projectiles by investigating enhanced maneuverability for range extension, terminal trajectory shaping, or engaging movers. High maneuverability aircraft and missiles have been in existence for many years. Classical and modern control techniques have been applied with much success to the missile problem [1,15,14,19,20,9,18]. Cost often associated with the sensor and actuation systems; however, it is a detractor for application of aircraft and missile technology to the gun-launched environment. The land warfare community requires a high volume of available fires and the projectiles are of one-time use in contrast to manned and unmanned aircraft. Additionally, maneuver authority is often limited in the gun application due to stowing aerodynamic stabilizing and control surfaces for tube launch and reduced dynamic pressure for aerodynamic control due to the frequent absence of a rocket motor. Components must be hardened to survive the gun launch event. Finally, the performance of low cost guidance, navigation, and control (GNC) technologies (e.g., initial measurement time, measurement calibration, measurement update rates, actuator bandwidth, and processor throughput) is stressed in the dynamic ballistic environment (high Mach number, short time-of-flight, high spin rate).

In this study we propose to solve the low cost, high maneuverability projectile problem using two fundamental ideas. The first core theme is to develop algorithms which reduce the actuator or sensor burden. Cost drivers in aerospace systems are often the sensor or actuation system. We seek to understand how carefully constructed software can accommodate poor performing hardware for gun-launched munitions. The second thesis is that high fidelity multidisciplinary modeling must be developed to perform simulations which consider all aspects of the problem concurrently. Understanding the coupling between modeling of the actuator input,

E-mail address: frank.e.fresconi.civ@mail.mil (F. Fresconi).

http://dx.doi.org/10.1016/j.ast.2014.12.007
1270-9638/Published by Elsevier Masson SAS.

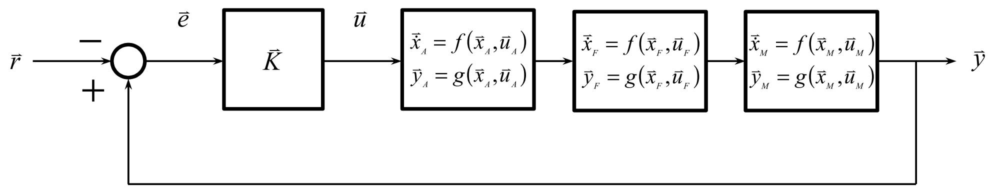

Fig. 1. Block diagram of nonlinear system dynamics with feedback control.

airframe response, and measurement output is critical to analyzing the cost-performance trades which define system requirements. Examining a portion of this problem in isolation as performed in past work does not yield cost driving technologies.

This paper is organized as follows. Nonlinear equations governing flight motion, actuator response, and measurements are derived. This paper describes these multidisciplinary nonlinear models in a comprehensive manner and formulates them for the present problem. Linearization and incorporation of flight, actuator, and measurement models into various system models which are critical to understanding guided flight behavior and underpins control design, are detailed. The overarching guidance and flight control strategy for low cost, enhanced maneuverability is sketched. The family of proportional guidance laws, which are based on the measurement models and enable interception of moving targets with minimal feedback measurements, is outlined. Flight control techniques are provided which utilize the system modeling and accommodate low cost actuation and measurement technologies. Characteristics of a high maneuverability airframe and low cost GNC system are given. Finally, linear flight control and nonlinear guidance and flight control simulation results demonstrate the implementation of the theory and efficacy of the GNC solution.

2. Theory

2.1. Problem formulation

The basic elements of a guided projectile are shown in the block diagram of Fig. 1. The nonlinear dynamics of the actuator, flight, and measurements are fed back and combined with a desired reference to yield an error. Control commands, formed by multiplying this error by a gain, influence the system dynamics to achieve the desired response.

High fidelity models of the actuator, flight, and measurements must be formulated and implemented in simulation to support the thesis of this work. These models are provided in subsequent sections.

2.2. Flight models

The flight model includes aerodynamics and flight dynamics. The reference frames and coordinate systems follow. The Earth coordinate system (subscript E) is used for the inertial frame and the body-fixed coordinate system (subscript B) is used for the body frame. These coordinate systems obey the right-hand rule and are related by the Euler angles for roll (ϕ), pitch (θ), and yaw (ψ) as shown in Fig. 2.

Applying trigonometry with the standard aerospace rotation sequence (Z–Y–X) yields the transformation matrix from quantities in body-fixed coordinates to Earth coordinates:

$$\vec{T}_{BE} = \begin{bmatrix} c_\theta c_\psi & s_\phi s_\theta c_\psi - c_\phi s_\psi & c_\phi s_\theta c_\psi + s_\phi s_\psi \\ c_\theta s_\psi & s_\phi s_\theta s_\psi + c_\phi c_\psi & c_\phi s_\theta s_\psi + s_\phi s_\psi \\ -s_\theta & s_\phi c_\theta & c_\phi c_\theta \end{bmatrix} \tag{1}$$

Maneuvering projectile flight is often achieved through moveable aerodynamic surfaces. Fig. 3 shows four moveable surfaces

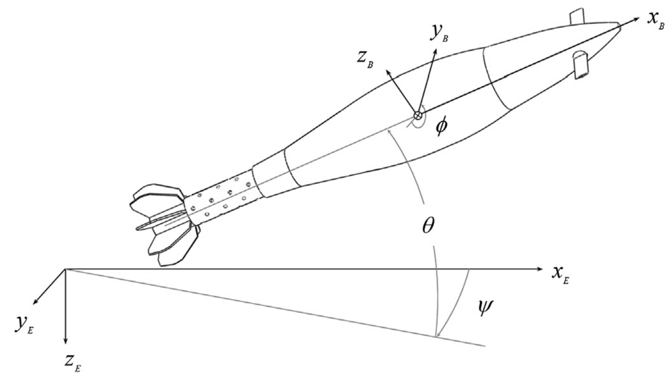

Fig. 2. Earth and body-fixed coordinate systems and Euler angles.

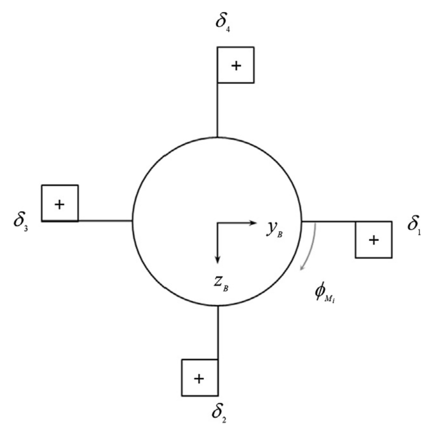

Fig. 3. Moveable aerodynamic surface numbering scheme and trailing edge deflection sign convention (viewed from projectile base).

equally distributed around the projectile; as well as the numbering scheme and sign convention associated with the trailing edge. The moveable aerodynamic surfaces are numbered starting with the surface with smallest roll angle and proceeding with increasing roll angle.

Individual moveable aerodynamic surfaces combine to yield effective roll, pitch, and yaw deflections. The drag deflections are not used in the maneuver scheme:

$$\begin{aligned} \delta_p &= \frac{1}{4}(-\delta_1 - \delta_2 - \delta_3 - \delta_4) \\ \delta_q &= \frac{1}{4}(\delta_1 - \delta_2 - \delta_3 + \delta_4) \\ \delta_r &= \frac{1}{4}(\delta_1 + \delta_2 - \delta_3 - \delta_4) \\ \delta_d &= \frac{1}{4}(\delta_1 - \delta_2 + \delta_3 - \delta_4) \end{aligned} \tag{2}$$

Rigid body projectile flight states are center-of-gravity position $[\,x\ y\ z\,]^T$, attitude $[\,\phi\ \theta\ \psi\,]^T$, body translational velocity $[\,u\ v\ w\,]^T$, and body rotational velocity $[\,p\ q\ r\,]^T$. Kinematics provides the relationships between motion in the body and inertial

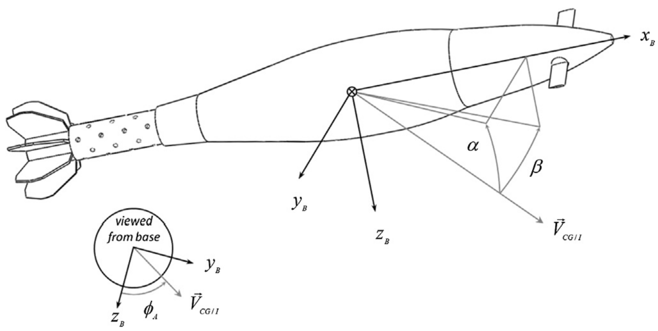

Fig. 4. Body-fixed coordinate system and aerodynamic angles.

frames. Translational and rotational kinematics for the body-fixed coordinate system are [13,10,16]

$$\begin{bmatrix} \dot{x} \\ \dot{y} \\ \dot{z} \end{bmatrix} = \begin{bmatrix} c_\theta c_\psi & s_\phi s_\theta c_\psi - c_\phi s_\psi & c_\phi s_\theta c_\psi + s_\phi s_\psi \\ c_\theta s_\psi & s_\phi s_\theta s_\psi + c_\phi c_\psi & c_\phi s_\theta s_\psi + s_\phi c_\psi \\ -s_\theta & s_\phi c_\theta & c_\phi c_\theta \end{bmatrix} \begin{bmatrix} u \\ v \\ w \end{bmatrix} \tag{3}$$

$$\begin{bmatrix} \dot{\phi} \\ \dot{\theta} \\ \dot{\psi} \end{bmatrix} = \begin{bmatrix} 1 & s_\phi t_\theta & c_\phi t_\theta \\ 0 & c_\phi & -s_\phi \\ 0 & s_\phi / c_\theta & c_\phi / c_\theta \end{bmatrix} \begin{bmatrix} p \\ q \\ r \end{bmatrix} \tag{4}$$

Newton's 2nd law may be applied to derive the dynamics of a rigid body projectile in flight. The translational dynamics may be expressed in body-fixed coordinates [13,10,16]

$$\begin{bmatrix} \dot{u} \\ \dot{v} \\ \dot{w} \end{bmatrix} = \frac{1}{m} \begin{bmatrix} X \\ Y \\ Z \end{bmatrix} - \begin{bmatrix} 0 & -r & q \\ r & 0 & -p \\ -q & p & 0 \end{bmatrix} \begin{bmatrix} u \\ v \\ w \end{bmatrix} \tag{5}$$

$$\begin{bmatrix} \dot{p} \\ \dot{q} \\ \dot{r} \end{bmatrix} = \vec{I}^{-1} \begin{bmatrix} L \\ M \\ N \end{bmatrix} - \vec{I}^{-1} \begin{bmatrix} 0 & -r & q \\ r & 0 & -p \\ -q & p & 0 \end{bmatrix} \vec{I} \begin{bmatrix} p \\ q \\ r \end{bmatrix} \tag{6}$$

The forces are comprised of aerodynamic and gravity ($\vec{F}_G^B = \vec{T}_{BE}^T [\,0\ \ 0\ \ g\,]^T$) terms. Moments are solely aerodynamic.

An illustration of the projectile with the body-fixed coordinate system is provided in Fig. 4.

Aerodynamic angles are computed based on the body-fixed velocity components. The pitch angle-of-attack (or sometimes just angle-of-attack) is defined below

$$\alpha = a\sin\left[\frac{w}{\sqrt{u^2 + w^2}}\right] \tag{7}$$

The yaw angle-of-attack (or sometimes sideslip angle) is

$$\beta = a\sin\left[\frac{v}{\sqrt{u^2 + v^2 + w^2}}\right] \tag{8}$$

The aerodynamic roll angle follows

$$\phi_A = a\tan\left[\frac{v}{w}\right] \tag{9}$$

Finally, the total angle-of-attack is the root-square-sum of the pitch and yaw angles-of-attack

$$\bar{\alpha} = \sqrt{\alpha^2 + \beta^2} \tag{10}$$

Total aerodynamic forces and moments are separated into rigid and moveable aerodynamic surfaces.

Rigid aerodynamic surface forces include static (linear and nonlinear) and dynamic terms. Symbols in parentheses indicate functional form of aerodynamic coefficients. The dynamic pressure is $Q = \frac{1}{2}\rho V^2$ and aerodynamic reference area is $S = \frac{\pi}{4} D^2$ where D is the projectile diameter and V is the total velocity

$$X_R = -QS\big[C_{X_0}(M) + C_{X_{\bar{\alpha}^2}}(M)\sin^2\bar{\alpha}\big] \tag{11}$$

$$\begin{aligned} Y_R = -QS\Big[& C_{Y_0}(M) + C_{Y_\beta}(M)\sin\beta \\ & + C_{Y_{\beta^3}}(M)\sin^3\beta + C_{Y_\alpha}(M)\sin\alpha \\ & + C_{Y_{p\alpha}}(M)\sin\alpha\frac{pD}{2V}\Big] \end{aligned} \tag{12}$$

$$\begin{aligned} Z_R = -QS\Big[& C_{Z_0}(M) + C_{Z_\alpha}(M)\sin\alpha \\ & + C_{Z_{\alpha^3}}(M)\sin^3\alpha + C_{Z_\beta}(M)\sin\beta \\ & + C_{Z_{p\beta}}(M)\sin\beta\frac{pD}{2V}\Big] \end{aligned} \tag{13}$$

Rigid aerodynamic surface moments include static (linear and nonlinear) and dynamic terms. The pitching moment accounts for a center-of-gravity (CG_N) which has been shifted from the center-of-gravity ($CG_{N,A}$) used to obtain the aerodynamic data. The center-of-gravity is measured from the nose and is given in units of calibers

$$L_R = QSD\Big[C_{l_0}(M, \bar{\alpha}, \phi_A, \delta_i) + C_{l_p}(M)\frac{pD}{2V}\Big] \tag{14}$$

$$\begin{aligned} M_R = QSD\Big[& C_{m_0}(M) + C_{m_\alpha}(M)\sin\alpha \\ & + C_{m_{\alpha^3}}(M)\sin^3\alpha + C_{m_q}(M)\frac{qD}{2V} \\ & + C_{m_\beta}(M)\sin\beta + C_{m_{p\beta}}(M)\sin\beta\frac{pD}{2V}\Big] \\ & - Z_R(CG_N - CG_{N,A})D \end{aligned} \tag{15}$$

$$\begin{aligned} N_R = QSD\Big[& -C_{n_0}(M) - C_{n_\beta}(M)\sin\beta - C_{n_{\beta^3}}(M)\sin^3\beta \\ & + C_{m_r}(M)\frac{rD}{2V} + C_{n_\alpha}(M)\sin\alpha \\ & + C_{n_{p\alpha}}(M)\sin\alpha\frac{pD}{2V}\Big] \\ & + Y_R(CG_N - CG_{N,A})D \end{aligned} \tag{16}$$

The following approach may be used to calculate moveable aerodynamic surface forces and moments for the ith blade. First, compute local velocity at each blade from center-of-pressure data (CP, measured in calibers forward of CG), blade geometry (ϕ_{M_i}), and rigid body states using the equation relating the velocity of two fixed points on a rigid body,

$$\vec{V}_{M_i/I} = \vec{V}_{CG/I} + \vec{\omega}_{B/I} \times \vec{r}_{CG \to CP_i} \tag{17}$$

where $\vec{V}_{CG/I} = [\,u\ \ v\ \ w\,]^T$, $\vec{\omega}_{B/I} = [\,p\ \ q\ \ r\,]^T$, and $\vec{r}_{CG \to CP_i} = D[\,(CP_X(M, \delta_{C_i}) + CG_N - CG_{N,A})\ \ CP_R\cos(\phi_{M_i})\ \ CP_R\sin(\phi_{Mi})\,]^T$. The axial and radial center-of-pressure of the moveable aerodynamic surface is a function of Mach number and lifting surface deflection angle δ_i.

Obtain local velocity at each blade in the moveable aerodynamic surface coordinate system using the transformation matrix:

$$\vec{T}_{BM_i} = \begin{bmatrix} 1 & 0 & 0 \\ 0 & \cos(\phi_{M_i}) & \sin(\phi_{M_i}) \\ 0 & -\sin(\phi_{M_i}) & \cos(\phi_{M_i}) \end{bmatrix} \tag{18}$$

$$\begin{bmatrix} u_{M_i}^{M_i} \\ v_{M_i}^{M_i} \\ w_{M_i}^{M_i} \end{bmatrix} = \vec{T}_{BM_i} \begin{bmatrix} u_{M_i}^B \\ v_{M_i}^B \\ w_{M_i}^B \end{bmatrix} \tag{19}$$

Calculate local blade angle-of-attack from the local velocity in each moveable aerodynamic surface coordinate system:

$$\alpha_{M_i} = \operatorname{asin}\left[\frac{w_{M_i}^{M_i}}{\sqrt{u_{M_i}^{M_i^2} + w_{M_i}^{M_i^2}}}\right] \tag{20}$$

Determine moveable aerodynamic surface aerodynamic coefficients:

$$C_X^{M_i} = C_{X_0}^M(M,\delta_i) + C_{X_{\alpha^2}}^M(M,\delta_i)\sin^2\alpha_{M_i} \tag{21}$$

$$C_l^{M_i} = C_{l_0}^M(M,\delta_i) \tag{22}$$

$$C_N^{M_i} = C_{N_0}^M(M,\delta_i) + C_{N_\alpha}^M(M,\delta_i)\sin\alpha_{M_i} + C_{N_{\alpha^3}}^M(M,\delta_i)\sin^3\alpha_{M_i} \tag{23}$$

$$C_m^{M_i} = C_{m_0}^M(M,\delta_i) + C_{m_\alpha}^M(M,\delta_i)\sin\alpha_{M_i} + C_{m_{\alpha^3}}^M(M,\delta_i)\sin^3\alpha_{M_i} \tag{24}$$

Compute moveable aerodynamic surface axial and normal force and roll and pitching moment:

$$X_{M_i} = -Q_{M_i} S C_X^{M_i} \tag{25}$$

$$L_{M_i} = Q_{M_i} S D C_l^{M_i} \tag{26}$$

$$Z_{M_i} = -Q_{M_i} S C_N^{M_i} \tag{27}$$

$$M_{M_i} = Q_{M_i} S D C_m^{M_i} - N_{M_i}(CG_N - CG_{N,A})D \tag{28}$$

Transform these forces and moments in the moveable aerodynamic surface coordinate system to the body-fixed coordinate system:

$$\begin{bmatrix} X_{M_i}^B \\ Y_{M_i}^B \\ Z_{M_i}^B \end{bmatrix} = \vec{T}_{BM_i}^T \begin{bmatrix} X_{M_i} \\ 0 \\ Z_{M_i} \end{bmatrix} \tag{29}$$

$$\begin{bmatrix} L_{M_i}^B \\ M_{M_i}^B \\ N_{M_i}^B \end{bmatrix} = \vec{T}_{BM_i}^T \begin{bmatrix} L_{M_i} \\ M_{M_i} \\ 0 \end{bmatrix} \tag{30}$$

The flight dynamics are linearized and cast into state space form for state dynamics ($\dot{\vec{x}}_F = \vec{A}_F \vec{x}_F + \vec{B}_F \vec{u}_F + \vec{F}_F$) and measurements ($\vec{y}_F = \vec{C}_F \vec{x}_F + \vec{D}_F \vec{u}_F$). The nonlinear equations of motion for projectile flight are linearized by making a few assumptions [13,3]. Off-diagonal inertia tensor terms are small compared with the diagonal terms. Gravity and products of dynamic states (i.e., u, v, w, p, q, r) are neglected. Total angle-of-attack is small and aerodynamic normal force and pitching moment trims, as well as side forces and side moments are neglected so that only linear terms remain in the aerodynamic model.

The state vector is defined:

$$\vec{x}_F = [\phi\ p\ q\ r\ \dot{v}\ \dot{w}]^T \tag{31}$$

The controls are the roll, pitch, and yaw deflections:

$$\vec{u}_F = [\delta_p\ \delta_q\ \delta_r]^T \tag{32}$$

The state transition matrix has the form below. The roll angle dynamics is incorporated by simple integration of the roll rate:

$$\vec{A}_F = \begin{bmatrix} 0 & 1 & 0 & 0 & 0 & 0 \\ 0 & \frac{QSD}{I_{xx}}\frac{D}{2V}C_{l_p} & 0 & 0 & 0 & 0 \\ 0 & 0 & \frac{QSD}{I_{zz}}\frac{D}{2V}C_{m_q} & 0 & 0 & \frac{mD}{I_{zz}}\frac{C_{m_\alpha}}{C_{Z_\alpha}} \\ 0 & 0 & 0 & -\frac{QSD}{I_{yy}}\frac{D}{2V}C_{m_r} & \frac{mD}{I_{yy}}\frac{C_{n_\beta}}{C_{Y_\beta}} & 0 \\ 0 & 0 & 0 & \frac{QS}{m}C_{Y_\beta} & -\frac{QS}{mV}C_{Y_\beta} & 0 \\ 0 & 0 & \frac{QS}{m}C_{Z_\alpha} & 0 & 0 & -\frac{QS}{mV}C_{Z_\alpha} \end{bmatrix} \tag{33}$$

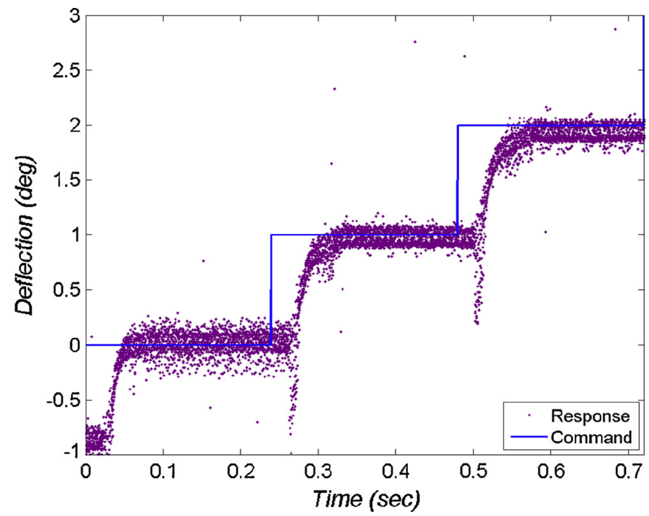

Fig. 5. Experimental actuator characterization.

The controls matrix follows

$$\vec{B}_F = \begin{bmatrix} 0 & 0 & 0 \\ \frac{QSD}{I_{zz}}C_{l_{\delta_p}} & 0 & 0 \\ 0 & \frac{QSD}{I_{zz}}C_{m_{\delta_q}} & 0 \\ 0 & 0 & -\frac{QSD}{I_{yy}}C_{n_{\delta_r}} \\ 0 & 0 & 0 \\ 0 & 0 & 0 \end{bmatrix} \tag{34}$$

The static roll moment appears as a steady-state term which is independent of the state and control vector:

$$\vec{F}_F = \begin{bmatrix} 0 \\ \frac{QSD}{I_{xx}}C_{l_0} \\ 0 \\ 0 \\ 0 \\ 0 \end{bmatrix} \tag{35}$$

The measurement matrix is simply the identity matrix ($\vec{C}_F = \vec{I}_{6\times 6}$) since feedback consists of accelerometers and angular rate sensors. All states are directly measureable except for roll angle, which would come from integrating an angular rate sensor or using magnetometer-only or some combination of magnetometer, accelerometer, and angular rate sensor in an observer. For this formulation $\vec{D}_F = 0$.

2.3. Actuator models

Actuator dynamics are modeled as a first order system with time delay and bias:

$$\tau\dot{\delta}(t) + \delta(t) = \delta_C(t - t_D) + \delta_B \tag{36}$$

This modeling approach is consistent with experimental characterizations of low cost actuation technology as seen in Fig. 5.

The transfer function form of a first order system is used to represent the first order actuator dynamics:

$$H_1(s) = \frac{1/\tau}{s + 1/\tau} \tag{37}$$

The Laplace transform of a time delay is provided below

$$\mathcal{L}\{\delta(t - t_D)\} = e^{-t_D s} \tag{38}$$

Pade approximants are used to represent the time delay:

$$f_P(s) \approx \frac{\sum_{k=0}^{N_P} p_k s^k}{\sum_{k=0}^{N_Q} q_k s^k} \tag{39}$$

The transfer function form of the Pade approximant is

$$H_D(s) = \frac{p_{N_P} s^{N_P} + \cdots + p_1 s + p_0}{q_{N_Q} s^{N_Q} + \cdots + q_1 s + 1} \tag{40}$$

Multiplying transfer functions yields Eq. (41). Assume that $N = N_P = N_Q$.

$$\begin{aligned} H_{D1}(s) &= H_D(s) H_1(s) \\ &= \frac{p_N s^N + \cdots + p_1 s + p_0}{\tau q_N s^{N+1} + (\tau q_{N-1} + q_N) s^N + \cdots + (\tau q_1 + q_2) s^2 + (\tau + q_1) s + 1} \end{aligned} \tag{41}$$

A state space model of the actuator with time delay and first order dynamics was constructed with the following state vector.

$$\vec{x}_{D1} = \begin{bmatrix} x^{(N)} & x^{(N-1)} & \dots & \dot{x} & x \end{bmatrix}^T \tag{42}$$

The control for the actuator is simply the deflection command.

$$\vec{u}_{D1} = \delta_C \tag{43}$$

Arranging terms in the transfer function provided in Eq. (41) with the definitions of the state and control vectors produces the state transition matrix:

$$\vec{A}_{D1} = \begin{bmatrix} -\frac{(\tau q_{N-1} + q_N)}{\tau q_N} & -\frac{(\tau q_{N-2} + q_{N-1})}{\tau q_N} & \dots & -\frac{(\tau + q_1)}{\tau q_N} & -\frac{1}{\tau q_N} \\ & \vec{I}_{N\times N} & & & \vec{0}_{N\times 1} \end{bmatrix} \tag{44}$$

Likewise, the control matrix can be formed:

$$\vec{B}_{D1} = \begin{bmatrix} \frac{1}{\tau q_N} \\ \vec{0}_{N\times 1} \end{bmatrix} \tag{45}$$

The measurement matrix is provided below ($\vec{D}_{D1} = 0$)

$$\vec{C}_{D1} = \begin{bmatrix} \frac{p_N}{\tau q_N} & \frac{p_{N-1}}{\tau q_N} & \cdots & \frac{p_1}{\tau q_N} & \frac{p_0}{\tau q_N} \end{bmatrix} \tag{46}$$

The state space model of the actuator with time delay and first order dynamics is for a given deflection. The flight model features roll, pitch, and yaw deflections. A comprehensive roll, pitch, yaw state space model may be constructed by building on the individual state space model outlined in Eqs. (42)–(46). The state vector and control vector are composed of three sub-vectors:

$$\vec{x}_A = [\vec{x}_{D1,p}^T \quad \vec{x}_{D1,q}^T \quad \vec{x}_{D1,r}^T]^T \tag{47}$$

$$\vec{u}_A = [\vec{u}_{D1,p}^T \quad \vec{u}_{D1,q}^T \quad \vec{u}_{D1,r}^T]^T \tag{48}$$

The state transition, control, and measurement matrices are assembled below

$$\vec{A}_A = \begin{bmatrix} \vec{A}_{D1,p} & \vec{0}_{N+1\times N+1} & \vec{0}_{N+1\times N+1} \\ \vec{0}_{N+1\times N+1} & \vec{A}_{D1,q} & \vec{0}_{N+1\times N+1} \\ \vec{0}_{N+1\times N+1} & \vec{0}_{N+1\times N+1} & \vec{A}_{D1,r} \end{bmatrix} \tag{49}$$

$$\vec{B}_A = \begin{bmatrix} \vec{B}_{D1,p} & \vec{0}_{N+1\times 1} & \vec{0}_{N+1\times 1} \\ \vec{0}_{N+1\times 1} & \vec{B}_{D1,q} & \vec{0}_{N+1\times 1} \\ \vec{0}_{N+1\times 1} & \vec{0}_{N+1\times 1} & \vec{B}_{D1,r} \end{bmatrix} \tag{50}$$

$$\vec{C}_A = \begin{bmatrix} \vec{C}_{D1,p} & \vec{0}_{1\times N+1} & \vec{0}_{1\times N+1} \\ \vec{0}_{1\times N+1} & \vec{C}_{D1,q} & \vec{0}_{1\times N+1} \\ \vec{0}_{1\times N+1} & \vec{0}_{1\times N+1} & \vec{C}_{D1,r} \end{bmatrix} \tag{51}$$

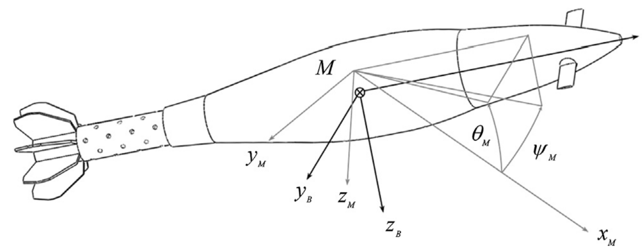

Fig. 6. Body-fixed and measurement coordinate systems.

2.4. Measurement models

Accelerometers, angular rate sensors, and imagers are the primary feedback measurements of interest. A schematic of an arbitrary sensor at point M with axes oriented relative to the body-fixed coordinate system is shown in Fig. 6.

The equation for the acceleration of two fixed points on a rigid body may be used to model the accelerometer off the projectile center-of-gravity. Integrated sensors suffer from errors in scale factor, misalignment, misposition, bias, and noise. An expression for an accelerometer corrupted by these errors can be developed:

$$\begin{aligned} \vec{f}_M^B = \vec{S}_M \vec{T}_{MB} \Bigg[& \frac{d\vec{V}_{CG/I}^B}{d} t + \vec{\omega}_{B/I} \times \vec{V}_{CG/I}^B - \vec{T}_{BE}^T [0 \quad 0 \quad g]^T \\ & + \dot{\vec{\omega}}_{B/I} \times (\vec{r}_{CG\to M} + \vec{\varepsilon}_{r_{CG\to M}}) + \vec{\omega}_{B/I} \times \vec{\omega}_{B/I} \\ & \times (\vec{r}_{CG\to M} + \vec{\varepsilon}_{r_{CG\to M}}) \Bigg] + \vec{\varepsilon}_B + \vec{\varepsilon}_N \end{aligned} \tag{52}$$

Angular rate sensors measure the angular velocity of the body with respect to the inertial frame in body-fixed coordinates. A model for angular rate sensors with scale factor, misalignment, bias, and noise errors is provided.

$$\vec{\omega}_{B/I,M} = \vec{S}_M \vec{T}_{MB} \vec{\omega}_{B/I} + \vec{\varepsilon}_B + \vec{\varepsilon}_N \tag{53}$$

The scale factor matrix for any sensor can be written as the identity matrix with a scale factor error unique to each orthogonal axis:

$$\vec{S}_M = \begin{bmatrix} 1 + \varepsilon_{M_{S,x_M}} & 0 & 0 \\ 0 & 1 + \varepsilon_{M_{S,y_M}} & 0 \\ 0 & 0 & 1 + \varepsilon_{M_{S,z_M}} \end{bmatrix} \tag{54}$$

The transformation from any sensor axes to the body coordinate system, including misalignment errors, is given below

$$\begin{aligned} & \vec{T}_{MB} \\ & = \begin{bmatrix} c_{(\theta_M + \varepsilon_{\theta_M})} c_{(\psi_M + \varepsilon_{\psi_M})} & -s_{(\psi_M + \varepsilon_{\psi_M})} & s_{(\theta_M + \varepsilon_{\theta_M})} c_{(\psi_M + \varepsilon_{\psi_M})} \\ c_{(\theta_M + \varepsilon_{\theta_M})} s_{(\psi_M + \varepsilon_{\psi_M})} & c_{(\psi_M + \varepsilon_{\psi_M})} & s_{(\theta_M + \varepsilon_{\theta_M})} s_{(\psi_M + \varepsilon_{\psi_M})} \\ -s_{(\theta_M + \varepsilon_{\theta_M})} & 0 & c_{(\theta_M + \varepsilon_{\theta_M})} \end{bmatrix} \end{aligned} \tag{55}$$

The bias error of some sensors may feature a term due to the power-up process and an additional term which drifts in flight and can be modeled with a Markov process:

$$\vec{\varepsilon}_B = \vec{\varepsilon}_{B,0} + \vec{\varepsilon}_{B,I} \tag{56}$$

The equation for the update of a Markov process follows

$$(\vec{\varepsilon}_{B,I})_{,i} = \rho (\vec{\varepsilon}_{B,I})_{,i-1} + \sigma_{B,I} \sqrt{1 - \rho^2} \mathcal{N}(0, 1) \tag{57}$$

with the correlation $\rho = e^{-\frac{t_s}{t_c}}$ where t_s is the sample time and t_c is the time constant.

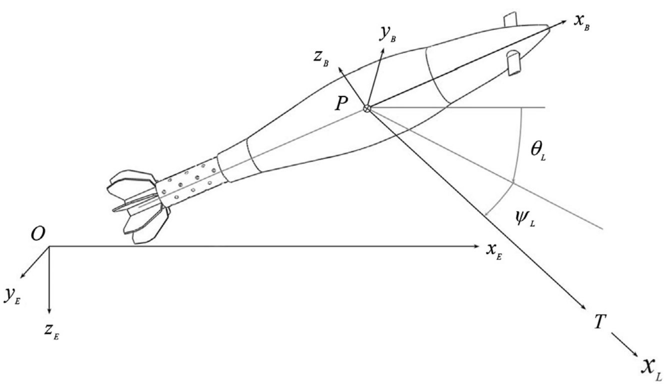

Fig. 7. Earth, line-of-sight, and body-fixed coordinate systems.

An imager model can be constructed by first defining the geometry in Fig. 7 between the Earth and line-of-sight coordinate systems associated with the inertial frame and the body-fixed coordinate system associated with the body frame.

The relative position of the target and projectile in the inertial frame is

$$\vec{r}^I_{PT} = \vec{r}^I_{OT} - \vec{r}^I_{OP} \tag{58}$$

The angles of the line-of-sight coordinate system with respect to the Earth coordinate system are

$$\psi_L^I = \tan^{-1}\left(\frac{r^I_{PT,y}}{r^I_{PT,x}}\right) \tag{59}$$

$$\theta_L^I = \tan^{-1}\left(\frac{r^I_{PT,z}}{\sqrt{{r^I_{PT,x}}^2 + {r^I_{PT,y}}^2}}\right) \tag{60}$$

The transformation matrix from Earth to line-of-sight coordinates may be formed based on the angles between the coordinate systems.

$$\vec{T}_{LE} = \begin{bmatrix} c_{\theta_L^I} c_{\psi_L^I} & -s_{\psi_L^I} & s_{\theta_L^I} c_{\psi_L^I} \\ c_{\theta_L^I} s_{\psi_L^I} & c_{\psi_L^I} & s_{\theta_L^I} s_{\psi_L^I} \\ -s_{\theta_L^I} & 0 & c_{\theta_L^I} \end{bmatrix} \tag{61}$$

The velocity of the target with respect to the projectile in the inertial frame is

$$\dot{\vec{r}}^I_{T/P} = \dot{\vec{r}}^I_{T/O} - \dot{\vec{r}}^I_{P/O} \tag{62}$$

The relative position in body-fixed coordinates can be written given the transformation matrix:

$$\vec{r}^B_{PT} = \vec{T}^T_{BE} \vec{r}^I_{PT} \tag{63}$$

Using the relative position in body-fixed coordinates the angles of the target centroid as seen by a strapdown seeker can be determined. Bias and noise may be added for modeling real-world measurements:

$$\psi_L^B = \tan^{-1}\left(\frac{r^B_{PT,y}}{r^B_{PT,x}}\right) + \varepsilon_B + \varepsilon_N \tag{64}$$

$$\theta_L^B = \tan^{-1}\left(\frac{r^B_{PT,z}}{\sqrt{{r^B_{PT,x}}^2 + {r^B_{PT,y}}^2}}\right) + \varepsilon_B + \varepsilon_N \tag{65}$$

Angular velocity of the line-of-sight coordinate system can be derived given the relation [7]:

$$\vec{\omega}_{L/I} = \frac{1}{|\vec{r}_{PT}|^2} \vec{r}_{PT} \times \dot{\vec{r}}_{T/P} \tag{66}$$

Substituting the expression for the relative position and velocity of the target with respect to the projectile in the Earth coordinate system in the above equation for the angular velocity yields the angular velocity components of the line-of-sight coordinate system:

$$\dot{\psi}_L^I = \frac{r^I_{PT,x} \dot{r}^I_{T/P,y} - r^I_{PT,y} \dot{r}^I_{T/P,x}}{{r^I_{PT,x}}^2 + {r^I_{PT,y}}^2} \tag{67}$$

$$\dot{\theta}_L^I = \frac{\sqrt{{r^I_{PT,x}}^2 + {r^I_{PT,y}}^2}\, \dot{r}^I_{T/P,z} - r^I_{PT,z} \sqrt{{\dot{r}^I_{T/P,x}}^2 + {\dot{r}^I_{T/P,y}}^2}}{{r^I_{PT,x}}^2 + {r^I_{PT,y}}^2 + {r^I_{PT,z}}^2} \tag{68}$$

Transforming the line-of-sight rates to the line-of-sight coordinate system and incorporating bias and noise errors characteristic of a practical imager yields the following expressions:

$$\dot{\theta}_L^L = \dot{\theta}_L^I c_{\psi_L^I} + \dot{\psi}_L^I s_{\theta L^I} s_{\psi_L^I} + \varepsilon_B + \varepsilon_N \tag{69}$$

$$\dot{\psi}_L^L = \dot{\psi}_L^I c_{\theta_L^I} + \varepsilon_B + \varepsilon_N \tag{70}$$

2.5. System models

Combined flight and actuator linear system dynamics models are provided for simulation and control design. The state and control vectors are made up of the flight and actuator with time delay and first order dynamics as derived earlier:

$$\vec{x}_{AF} = \begin{bmatrix} \vec{x}_F^T & \vec{x}_A^T \end{bmatrix}^T \tag{71}$$

$$\vec{u}_{AF} = \begin{bmatrix} \vec{u}_F^T & \vec{u}_A^T \end{bmatrix}^T \tag{72}$$

The state transition matrix is composed of the flight and actuator state transition matrix and an additional term in the top-right of the matrix due to the coupling as given in Eq. (73):

$$\vec{A}_{AF} = \begin{bmatrix} \vec{A}_F & \vec{B}_F \vec{C}_A \\ \vec{0}_{3(N+1)\times 6} & \vec{A}_A \end{bmatrix} \tag{73}$$

The coupling reduces the controls matrix to the following equation. The top-left portion of the matrix is a block of zeros since the coupling has picked off the controls matrix for the flight model:

$$\vec{B}_{AF} = \begin{bmatrix} \vec{0}_{6\times 3} & \vec{0}_{6\times 3} \\ \vec{0}_{3(N+1)\times 3} & \vec{B}_A \end{bmatrix} \tag{74}$$

The $\vec{F}_{AF}$ vector is a concatenation of the $\vec{F}_F$ vector followed by a row of zeros the length of $\vec{x}_A$. Lastly, the measurement matrix for the system is provided

$$\vec{C}_{AF} = \begin{bmatrix} \vec{C}_F & \vec{0}_{6\times 3(N+1)} \\ \vec{0}_{3\times 6} & \vec{C}_A \end{bmatrix} \tag{75}$$

Another useful linear system model is for the flight dynamics and first order actuator dynamics without time delay. The state vector for this system is defined:

$$\vec{x}_{F1} = \begin{bmatrix} \phi & p & q & r & \dot{v} & \dot{w} & \delta_p & \delta_q & \delta_r \end{bmatrix}^T \tag{76}$$

The control vector is given below

$$\vec{u}_{F1} = \begin{bmatrix} \delta_{C,p} & \delta_{C,q} & \delta_{C,r} \end{bmatrix}^T \tag{77}$$

The state transition matrix is formed based on the dynamic modeling performed above:

$$\vec{A}_{F1} = \begin{bmatrix} 0 & 1 & 0 & 0 & 0 & 0 & 0 & 0 & 0 \\ 0 & \frac{QSD}{I_{xx}}\frac{D}{2V}C_{l_p} & 0 & 0 & 0 & 0 & \frac{QSD}{I_{zz}}C_{l_{\delta_p}} & 0 & 0 \\ 0 & 0 & \frac{QSD}{I_{zz}}\frac{D}{2V}C_{m_q} & 0 & 0 & \frac{mD}{I_{zz}}\frac{C_{m\alpha}}{C_{Z\alpha}}0 & \frac{QSD}{I_{zz}}C_{m_{\delta_q}} & 0 & \\ 0 & 0 & 0 & -\frac{QSD}{I_{yy}}\frac{D}{2V}C_{m_r} & \frac{mD}{I_{yy}}\frac{C_{n_\beta}}{C_{Y_\beta}} & 0 & 0 & 0 & -\frac{QSD}{I_{yy}}C_{n_{\delta_r}} \\ 0 & 0 & 0 & \frac{QS}{m}C_{Y\beta} & -\frac{QS}{mV}C_{Y_\beta} & 0 & 0 & 0 & 0 \\ 0 & 0 & \frac{QS}{m}C_{Z_\alpha} & 0 & 0 & -\frac{QS}{mV}C_{Z_\alpha} & 0 & 0 & 0 \\ 0 & 0 & 0 & 0 & 0 & 0 & -\frac{1}{\tau_p} & 0 & 0 \\ 0 & 0 & 0 & 0 & 0 & 0 & 0 & -\frac{1}{\tau_q} & 0 \\ 0 & 0 & 0 & 0 & 0 & 0 & 0 & 0 & -\frac{1}{\tau_r} \end{bmatrix} \tag{78}$$

The control matrix takes the following form

$$\vec{B}_{F1} = \begin{bmatrix} \vec{0}_{6\times1} & \vec{0}_{6\times1} & \vec{0}_{6\times1} \\ \frac{1}{\tau_p} & 0 & 0 \\ 0 & \frac{1}{\tau_q} & 0 \\ 0 & 0 & \frac{1}{\tau_r} \end{bmatrix} \tag{79}$$

Again, the static roll moment is included:

$$\vec{F}_{F1} = \begin{bmatrix} 0 \\ \frac{QSD}{I_{xx}}C_{l_0} \\ \vec{0}_{7\times1} \end{bmatrix} \tag{80}$$

Finally, the measurement matrix is shown:

$$\vec{C}_{F1} = \begin{bmatrix} \vec{I}_{6\times6} & \vec{0}_{6\times3} \\ \vec{0}_{3\times6} & \vec{0}_{3\times3} \end{bmatrix} \tag{81}$$

3. Guidance and flight control

The proportional navigation law with gravity compensation is given below in body-fixed components. This equation is one representation of the proportional navigation family of guidance laws; there are many different variants in the literature [21].

$$\begin{bmatrix} a_C^{X_B} \\ a_C^{Y_B} \\ a_C^{Z_B} \end{bmatrix} = N_G V_C \vec{T}_{BE}^T \vec{T}_{LE} \begin{bmatrix} 0 \\ \dot{\psi}_L^L \\ \dot{\theta}_L^L \end{bmatrix} + \vec{T}_{BE}^T \begin{bmatrix} 0 \\ 0 \\ -g \end{bmatrix} \tag{82}$$

In practice, only lateral acceleration can be altered with aerodynamic control, range-rate measurements or heuristics supply the closing velocity, angular rate sensors or magnetometers supply attitude, and an imager or spot detector provide the line-of-sight rates.

The linear system model without time delay that was derived earlier can be used for control purposes. The state space model can be defined with $\vec{x} = \vec{x}_{F1}$, $\vec{u} = \vec{u}_{F1}$, $\vec{A} = \vec{A}_{F1}$, $\vec{B} = \vec{B}_{F1}$, $\vec{F} = \vec{F}_{F1}$, $\vec{C} = \vec{C}_{F1}$, and $\vec{D} = \vec{D}_{F1}$.

The nonlinear measurement models outlined above can be utilized to express the six feedback states.

$$\vec{y} = \begin{bmatrix} \phi_M & \vec{\omega}_{B/I,M} & f_M^B(2) & -f_M^B(3) \end{bmatrix}^T \tag{83}$$

For this problem the desired response is to regulate the roll angle to any of four angles determined by symmetry (based on flying skid-to-turn in an "X" configuration), maintain zero roll rate, pitch rate, and yaw rate, and achieve the lateral accelerations dictated by the guidance law. Mathematically, the reference signal is expressed as

$$\vec{r} = \begin{bmatrix} 0 & 0 & 0 & 0 & a_C^{Y_B} & -a_C^{Z_B} \end{bmatrix}^T \tag{84}$$

Manipulation of the roll angle error signal is accomplished by the following function to ensure that the roll angle is controlled to the closest symmetry location

$$e_\phi = \begin{cases} (\phi_M \ modulo\ \frac{\pi}{2}) - \frac{\pi}{4} & \text{if } \phi_M \ modulo\ \pi < \frac{\pi}{2} \\ -(\phi_M \ modulo\ \frac{\pi}{2}) + \frac{\pi}{4} & \text{if } \phi_M \ modulo\ \pi \geq \frac{\pi}{2} \end{cases} \tag{85}$$

A variety of control techniques may be applied given the linear actuator and flight dynamics, measurement models, and feedback control structure presented. A linear quadratic regulator, derived using optimal control theory, was chosen [4]. In the linear quadratic regulator development, the control command is based on minimizing a cost function:

$$J = \int_0^\infty \left(\vec{x}^T \vec{\mathbf{Q}} \vec{x} + \vec{u}^T \vec{\mathbf{R}} \vec{u}\right) dt \tag{86}$$

The weightings for the tracking error $\vec{\mathbf{Q}}$ and control effort $\vec{\mathbf{R}}$ are positive semi-definite and allow the designer to balance tracking each desired state with specific control demand. The control law that minimizes the cost function is

$$\vec{u} = -\vec{K}\vec{x} \tag{87}$$

The gain matrix can be found through the control effort weighting, the controls matrix, and the matrix $\vec{P}$:

$$\vec{K} = \vec{\mathbf{R}}^{-1} \vec{B}^T \vec{P} \tag{88}$$

The $\vec{P}$ matrix is obtained by solving the algebraic matrix Riccati equation:

$$\vec{A}^T \vec{P} + \vec{P}\vec{A} - \vec{P}\vec{B}\vec{\mathbf{R}}^{-1}\vec{B}^T\vec{P} + \vec{\mathbf{Q}} = 0 \tag{89}$$

Delays between the time of commanded control and when the effect of control is realized in the system dynamics occur due to a variety of physical processes and can add significant difficulty to the control problem. Additionally, the time delay magnitude may be higher when utilizing low cost technologies, such as commercial-off-the-shelf servomechanisms. The Smith predictor is a control strategy for dealing with time delays [17]. A block diagram of the Smith predictor algorithm for the projectile problem is given in Fig. 8. The linear system model without and with time delay are used in augmenting the feedback system and the nonlinear actuator, flight, and measurement models represent ground truth in simulation. Measurements are a function of the flight states and controls.

The basic idea of the Smith predictor is that a model of the system dynamics with time delay can be used to negate the true system dynamics with time delay. Controllers that do not inherently consider the time delay (such as the linear quadratic regulator) can then be applied since the resulting feedback signal has the time delay effectively removed.

The linear system models without and with time delay are propagated forward in time in implementation of the Smith predictor. Feedback is altered by the following equation

$$\vec{u} = \vec{K}(\vec{y}_{F1} + \vec{y}_M - \vec{y}_{AF} - \vec{r}) \tag{90}$$

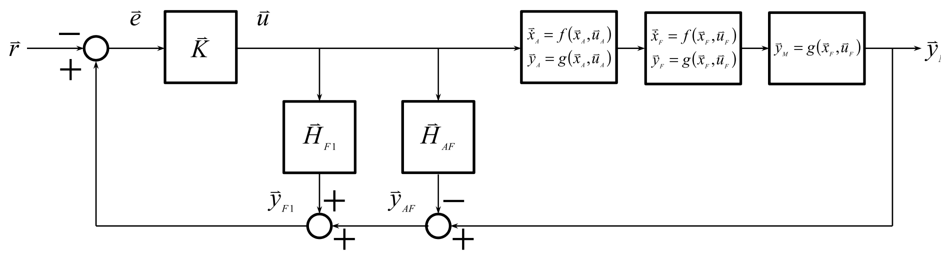

Fig. 8. Smith predictor.

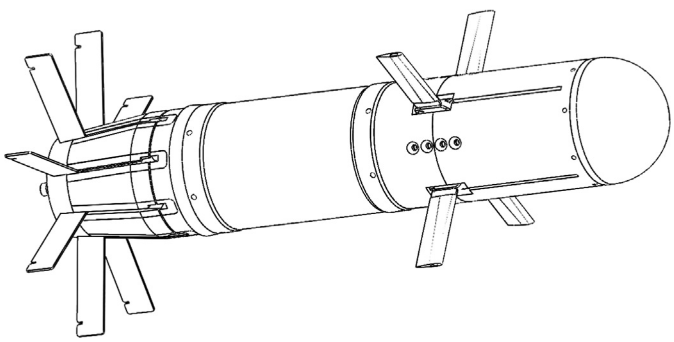

Fig. 9. High maneuverability airframe.

Table 1
Mass properties.

Property	μ	Unit	σ	Unit
D	0.083	m	0.12	%
CG_N	0.285	m from nose	0.12	%
L	0.427	m	0.12	%
m	2.65	kg	0.41	%
I_{XX}	0.0034	$\text{kg}\,\text{m}^2$	0.88	%
$I_{YY} = I_{ZZ}$	0.0388	$\text{kg}\,\text{m}^2$	0.71	%

Table 2
Aerodynamic data at Mach 0.65 for $CG_{N,A} = 0.264$ m from nose.

Property	μ	Unit	σ	Unit
C_{X_0}	0.366	–	0.86	%
$C_{Y_\beta} = C_{Z_\alpha}$	10.314	1/rad	1	%
$C_{n_\beta} = C_{m_\alpha}$	−5.642	1/rad	2	%
C_{l_0}	0.0889	–	5	%
C_{l_p}	−11.384	–	5	%
$C_{m_q} = C_{n_r}$	−88.820	–	15	%
CP_X	1.459	calibers forward CG	2	%
CP_R	0.781	calibers from spin axis	2	%
$C^M_{X_0}$	0.0042	–	0.86	%
$C^M_{l_\alpha}$	−1.075	1/rad	5	%
$C^M_{N_\alpha}$	1.377	1/rad	1	%
$C^M_{m_\alpha}$	2.010	1/rad	2	%

4. System characteristics

Models for the actuator, flight, and measurements are driven by input system characteristic data. Performing simulations with appropriate mean and uncertainty in the system characteristics is critical to assessing guided flight performance. An illustration of a fin-stabilized, canard-controlled projectile housing the required sensors is presented at the top of Fig. 9.

The mass properties (mean and uncertainty) of this projectile are given in Table 1.

The launch and flight is subsonic. Some aerodynamic data for this airframe, as obtained from computational fluid dynamics simulations at Mach 0.65, is provided in Table 2.

Table 3
Actuator properties.

Property	μ	Unit	σ	Unit
τ	0.015	sec	20	%
t_D	0.030	sec	20	%
δ_B	–	–	1	deg

Table 4
Measurement properties.

Property	σ	Unit
$\varepsilon_{\theta_M} = \varepsilon_{\psi_M}$ (integrated misalignment)	0.5	deg
$\varepsilon_{r_{CG \to M}}$ (accelerometer)	0.0005	m
ε_{M_S} (accelerometer)	1.0	%
$\varepsilon_{B,0}$ (accelerometer)	1.0	m/s^2
ε_N (accelerometer)	0.1	m/s^2
ε_{M_S} (gyroscope)	2.1	%
$\varepsilon_{B,0}$ (gyroscope)	0.016	Hz
ε_N (gyroscope)	0.016	Hz
ε_B (imager boresight angles)	10	deg
ε_B (imager boresight angular rates)	0.0016	Hz
ε_N (imager boresight angular rates)	0.00016	Hz
ε_B (closing velocity)	0.1	m/s

Table 5
Launch variation.

Property	σ	Unit
ϕ	2π (uniform)	rad
θ	0.004014	rad
ψ	0.005411	rad
V	3.7	m/s
p	0.16	Hz
q	0.16	Hz
r	0.16	Hz
Target position	2.0	m
Target velocity	0.5	m/s

Actuator parameters given in Table 3 are representative of low cost, high volume manufactured servomechanisms. The update rate of the actuator was 500 Hz.

Feedback measurement characteristics are given in Table 4. Feedback update rate was 1000 Hz.

The variation in the initial conditions of the projectile and target are provided in Table 5. The target was modeled as a constant velocity, straight-line motion.

The controller parameters, found via stability analysis and tuning in the linear and nonlinear simulations are given in Table 6. The update rate of the flight controller was 500 Hz.

5. Results and discussion

The theory for the flight, actuator, and measurements were implemented in simulation to assess multidisciplinary cost-performance drivers and demonstrate how control algorithms may be used to reduce the actuator burden.

A stability analysis was undertaken. The eigenvalues in Fig. 10 were shaped for desired performance with the linear flight and

Table 6
Controller properties.

Property	Value
$\mathbf{R_w}$	10
$\mathbf{Q_w}$	0.05
$\mathbf{Q_\phi}$	100
$\mathbf{Q_p}$	0.05
$\mathbf{Q_q}$	10
$\mathbf{Q_r}$	10
$\mathbf{Q_{\dot{v}}}$	0.8
$\mathbf{Q_{\dot{w}}}$	0.8

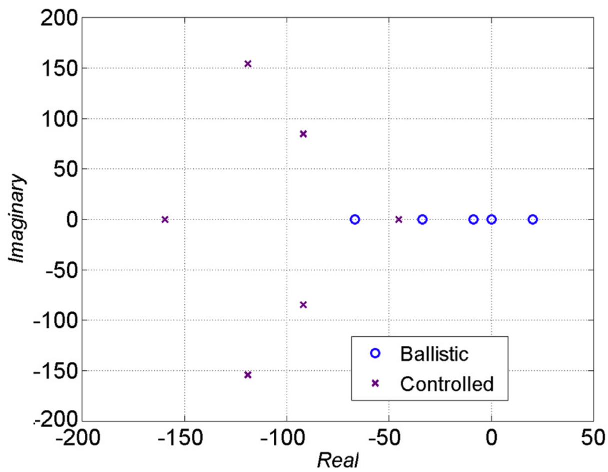

Fig. 10. Characteristic values of linear system dynamics.

first order actuator model and system characteristics provided earlier. Inspection of the controlled and uncontrolled (ballistic) data illustrates how the control increases the damping and frequency of the response. This airframe is statically unstable therefore the uncontrolled response has positive real roots.

Linear simulations were performed to assess ballistic flight behavior and further tune the flight controller for the desired performance. The flight control algorithm was implemented in simulation. The results in Figs. 11–13 show performance of the linear quadratic regulator for a time delay of zero with nominal initial conditions.

The roll dynamics and control demand are provided in Fig. 11. Inspection of the roll angle data illustrates the achieved roll angle, the roll error signal and the desired roll signal. The roll angle error signal has been manipulated as outlined previously to maintain configuration symmetry of the moveable aerodynamic surfaces (i.e., the error is not the difference between the achieved and desired signals as shown in the plot). The roll rate plot provides similar data (desired, achieved, error). The commanded and achieved (based on actuator dynamics) roll deflection angle is also given. Overall, this control design yields satisfactory roll response with reasonable control effort. Adequate control of the roll dynamics is necessary for proper pitch and yaw control.

Fig. 12 shows the pitch dynamics for a desired pitch acceleration of 50 m/s^2. Pitch deflections oscillate initially to sufficiently damp angular rate. The desired pitch acceleration is tracked to less than 1 m/s^2 error by deflecting in pitch to about 5 deg.

A Monte Carlo study was performed to assess the influence of system uncertainties on the controlled flight performance with $t_D = 0$. The initial conditions, mass properties, aerodynamic coefficients, actuator characteristics, and measurement errors were

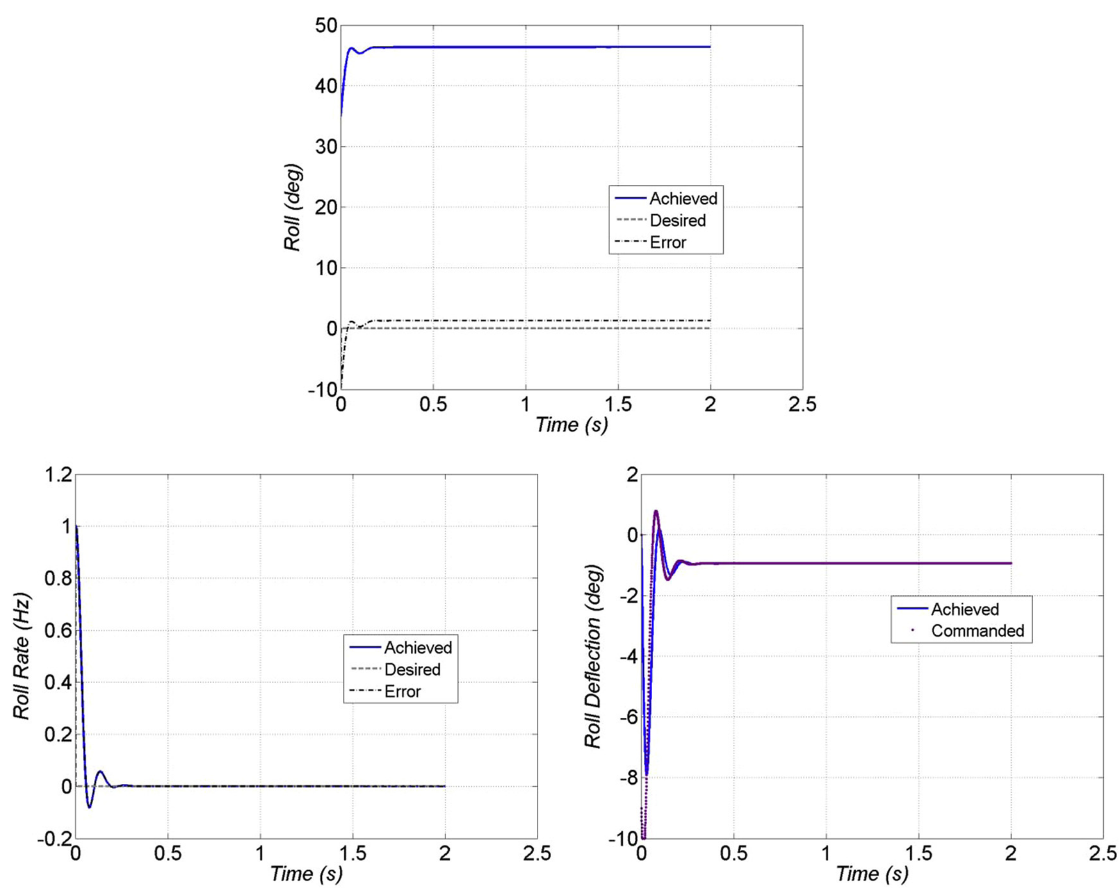

Fig. 11. Linear roll system dynamics response and deflection commands (linear quadratic regulator control with $t_D = 0$).

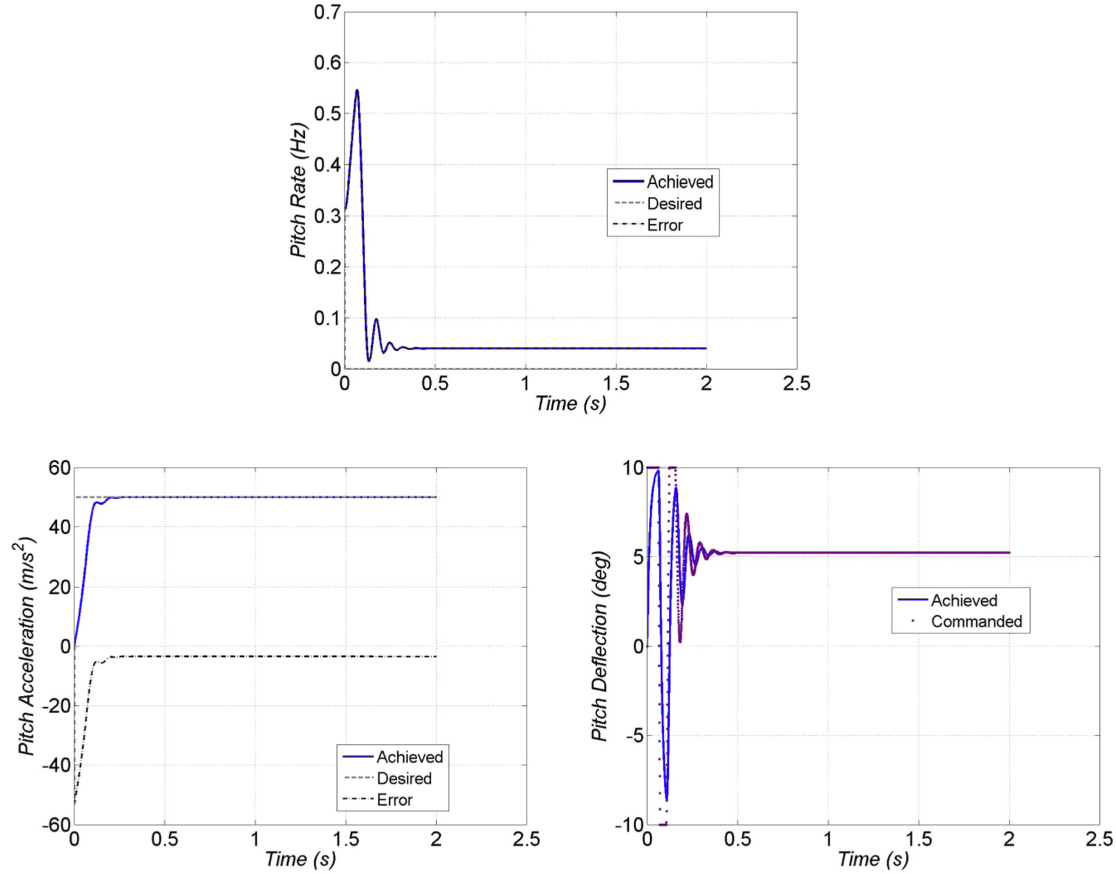

Fig. 12. Linear pitch system dynamics response and deflection commands (linear quadratic regulator control with $t_D = 0$).

varied according to the parameter distributions supplied earlier. Linear simulations were run for each Monte Carlo trial for 1.5 s and the error between the desired and achieved state were tabulated. The mean (shown in solid circle) and +/− standard deviation (shown in "X") of these errors is given in Fig. 13. Different colors in the figure represent different states. The error budget for the system uncertainties was scaled by different factors $(0.1, 1, 2, 3)$ for trend analysis. With the exception of roll angle, the mean controlled state errors do not vary much. Roll angle is biased about 1–2 deg due to the fin cant. This effect could easily be accounted for with some feedforward action. The standard deviation of the errors for all states but roll, pitch, and yaw rates grows linearly with the error budget factor. The angular rate errors are low since the control is effective and damping moments are active.

The pitch dynamics are isolated to investigate the effects of time delay. Linear simulations were performed with a non-zero time delay. The unstable behavior of the linear quadratic regulator for non-zero time delay is evident in Fig. 14. Commanded pitch deflections oscillate back and forth at the saturation levels and produce poor tracking in pitch acceleration and pitch rate.

The value of modeling the system dynamics with time delay in the controller is apparent when using the Smith predictor. The Smith predictor was implemented in simulation and linear results with non-zero time delay are provided in Fig. 15. Augmenting the linear quadratic regulator with the Smith predictor yields a satisfactory system response, especially when compared with the data in Fig. 14. The desired pitch rate and pitch acceleration is met with reasonable pitch deflection commands.

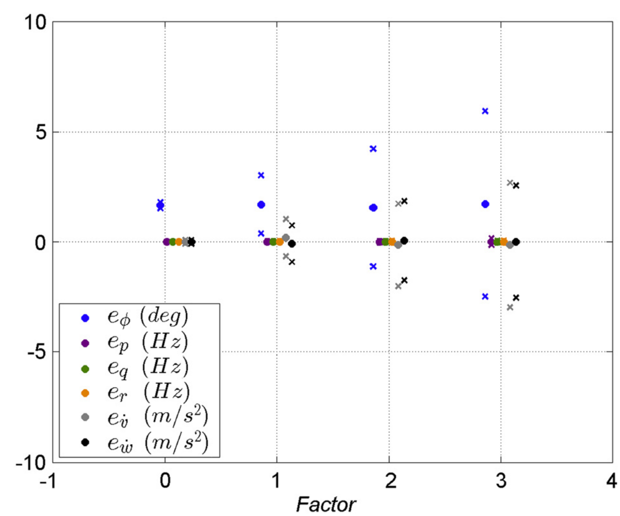

Fig. 13. Linear system simulation – Monte Carlo response trades. (For interpretation of the references to color in this figure, the reader is referred to the web version of this article.)

Nonlinear system simulations were conducted to further investigate the flight control and demonstrate guidance performance against moving targets. The projectile was launched at sea level and muzzle velocity of 250 m/s with the target initially located along the line-of-fire 1000 m downrange. The target was moving 5 m/s in the crossrange direction. In addition to the aerodynamics, mass properties, actuator, and feedback measurement characteristics perturbed in the linear Monte Carlo simulations, the atmo-

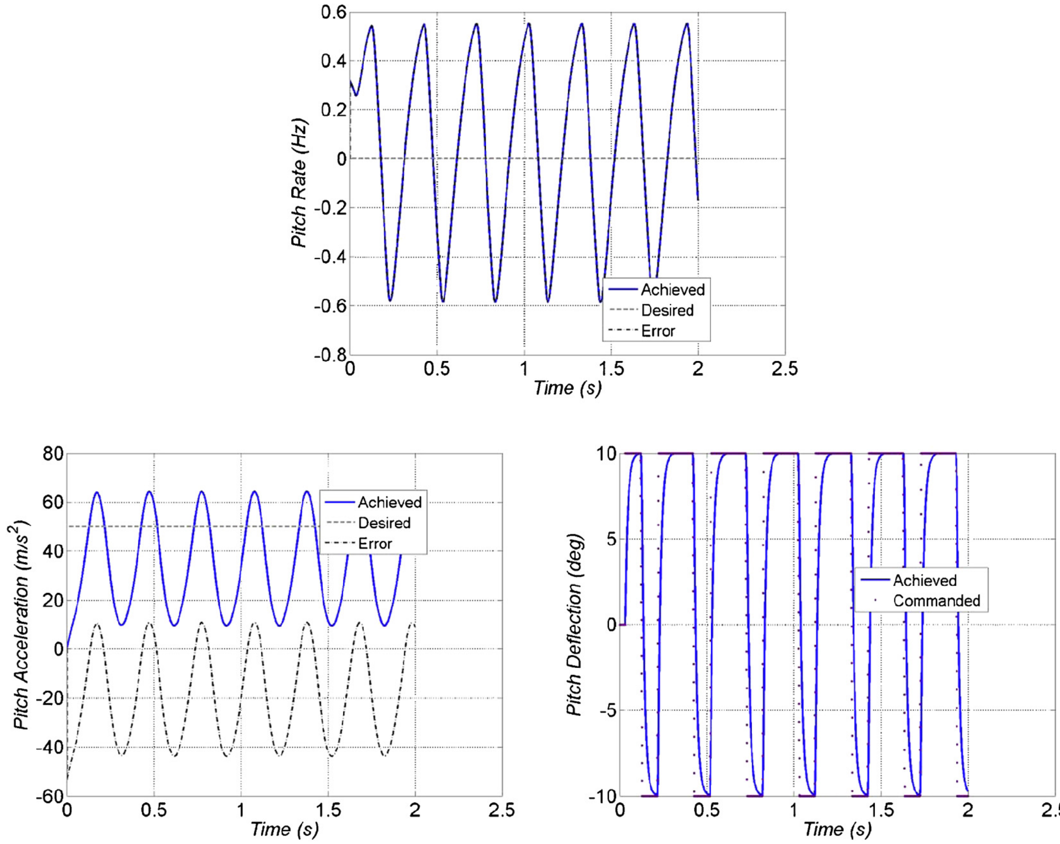

Fig. 14. Linear pitch system dynamics response and deflection commands (linear quadratic regulator control with $t_D \neq 0$).

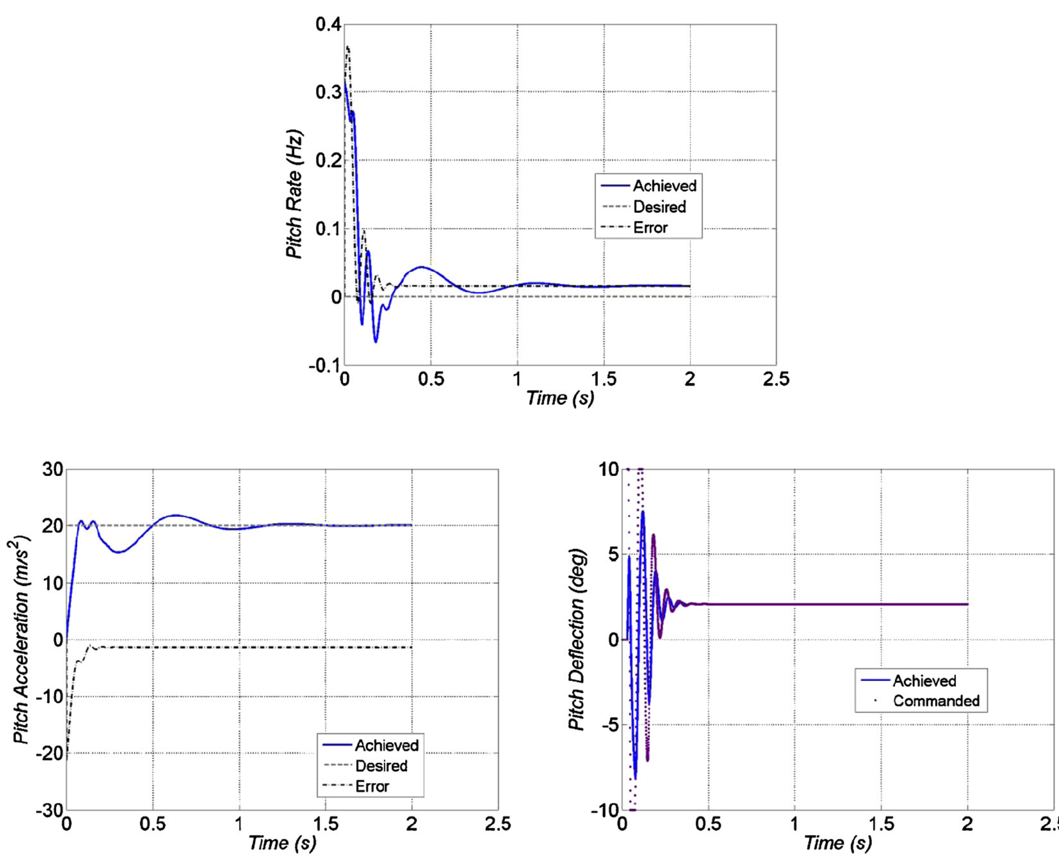

Fig. 15. Linear pitch system dynamics response and deflection commands (linear quadratic regulator and Smith control with $t_D \neq 0$).

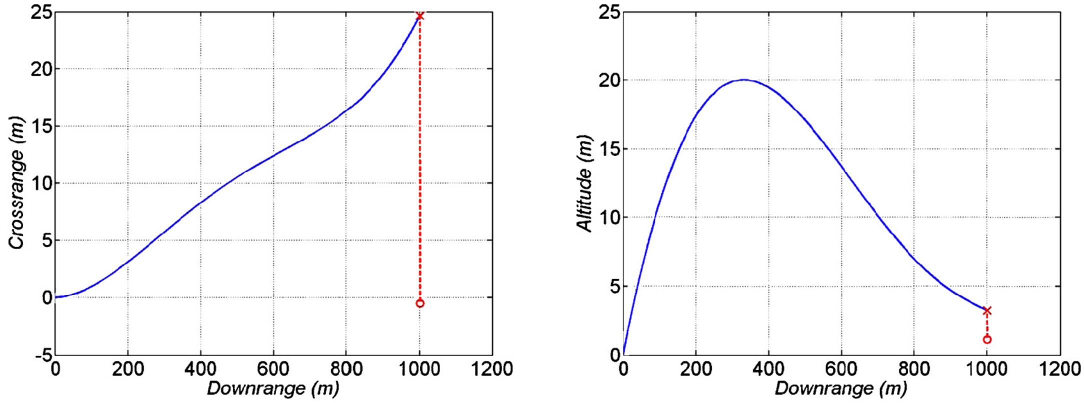

Fig. 16. Nonlinear system simulation – trajectory.

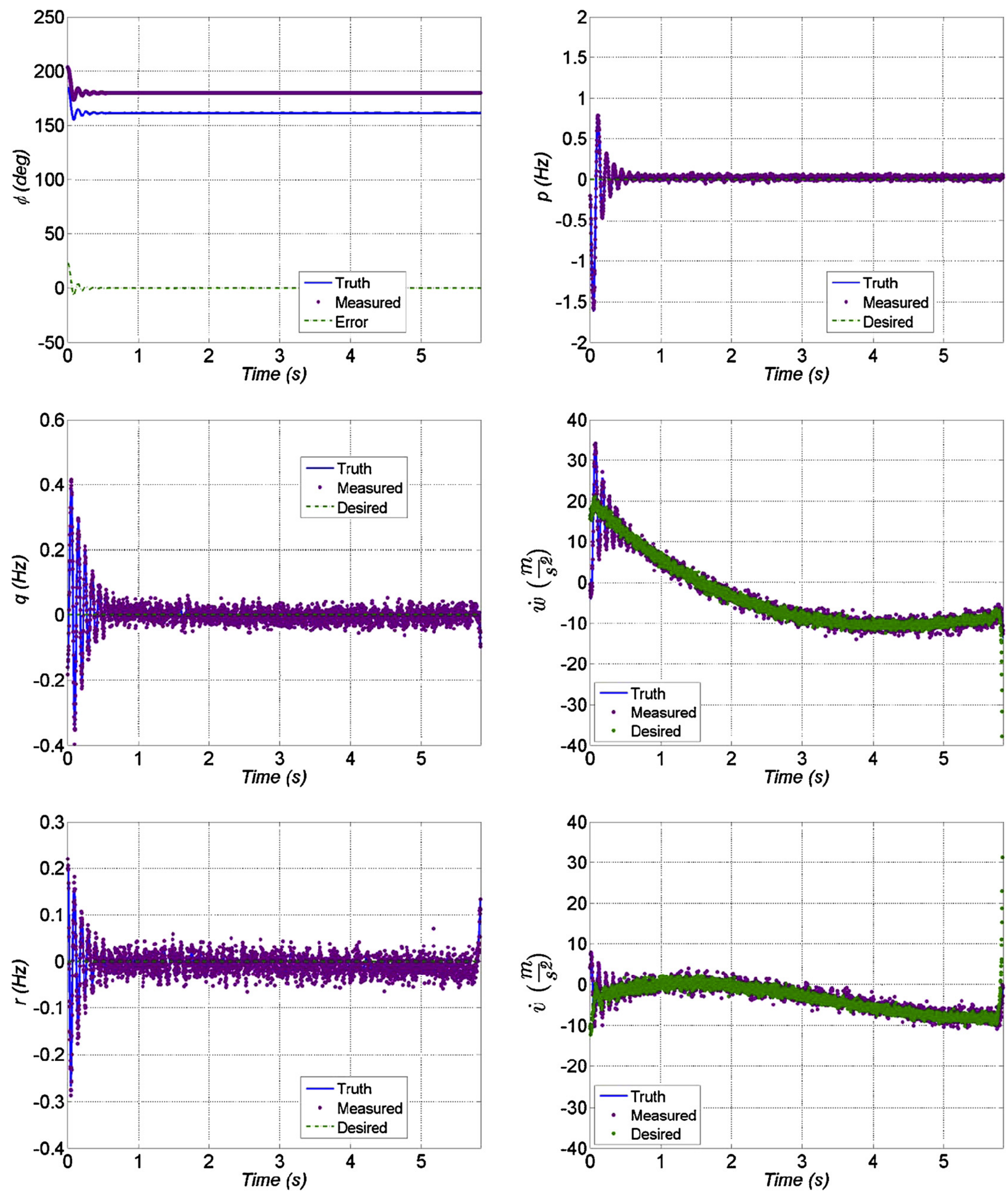

Fig. 17. Nonlinear system simulation – roll, pitch, yaw system dynamics response.

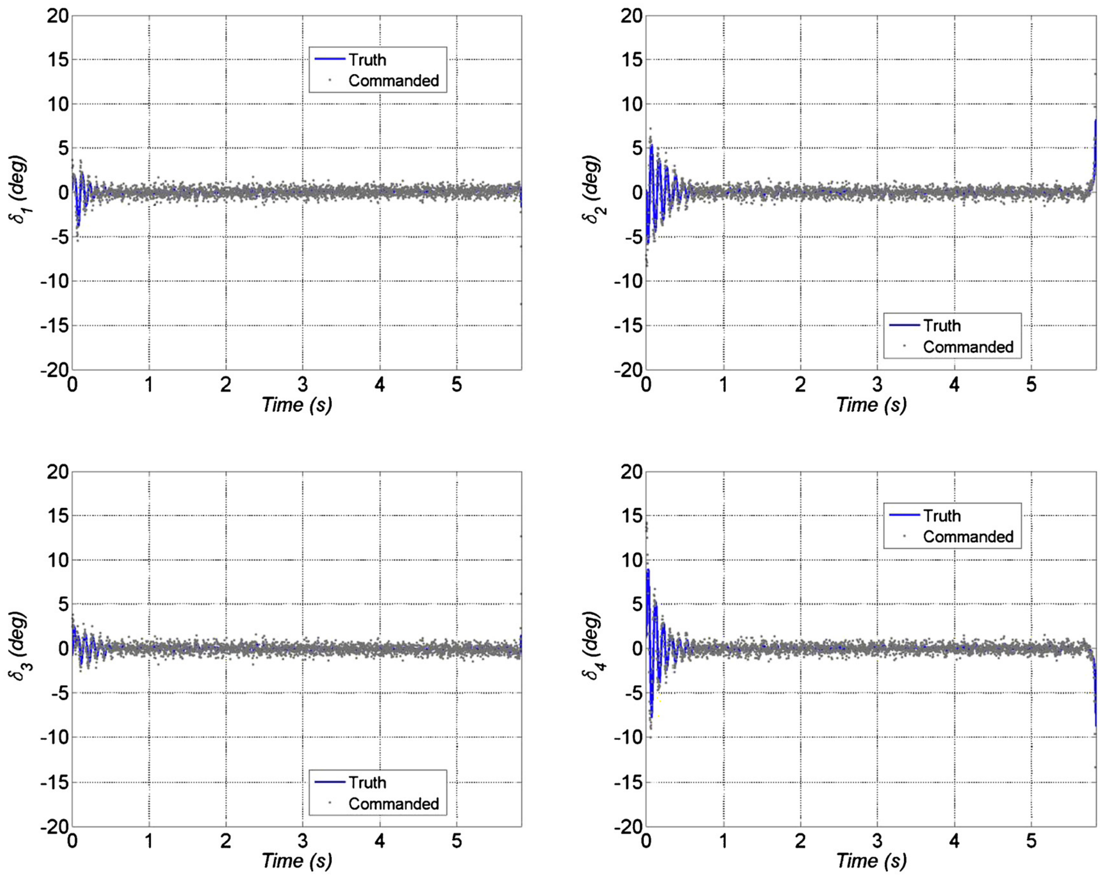

Fig. 18. Nonlinear system simulation – individual canard deflection commands.

sphere (e.g., density, sound speed, wind magnitude and direction) was also varied in nonlinear system simulations.

A sample Monte Carlo trajectory with system characteristics outlined previously is provided in Fig. 16. The projectile (solid line) maneuvers toward the target (dotted line) with a small point-of-closest-approach. The target moves about 25 m in crossrange over approximately 6 s of projectile time-of-flight. The projectile does not decrease much in Mach over the 5 s flight. The angles-of-attack, dictated primarily by the desired lateral accelerations from the guidance law, are less than 5 deg and well within the bounds of the high maneuverability airframe.

The performance of the roll, pitch, and yaw control in the nonlinear simulations is provided in Fig. 17. The desired, achieved, and measured (i.e., corrupted truth) states are given in the relevant plots for all nonlinear system simulations. Measurement corruption (e.g., noise) typical of low cost devices is evident when comparing measured and truth data. Both roll angle and roll rate feature good response. Pitch and yaw rates are controlled to near zero as desired which is within the measurement uncertainty. Comparing the desired pitch and yaw accelerations, computed from the proportional navigation guidance law with errors in the line-of-sight rate estimates, and the achieved and measured pitch and yaw accelerations shows errors less than 1 m/s^2 error of the majority of flight. The feedback measurement noise illustrated in the plots could be mitigated with an estimation algorithm such as a Kalman filter.

The roll, pitch, and yaw deflection commands are turned into individual moveable aerodynamic surface commands as outlined earlier. The individual commands and truth response are provided in Fig. 18. Roll deflection angles were about 1 deg to counteract the fin cant after the initial roll control action near launch. The deflections are larger near launch due to initial control action and vary slowly with amplitudes under 5 deg throughout flight. Amplitude increases sharply just prior to intercept. Overall, modest deflections are necessary to achieve the desired pitch/yaw rates and pitch/yaw acceleration response. Measurement errors (mainly noise) propagate through the controller and appear as high frequency variation in the canard commands. Filtering could be applied if these effects were harmful to overall performance.

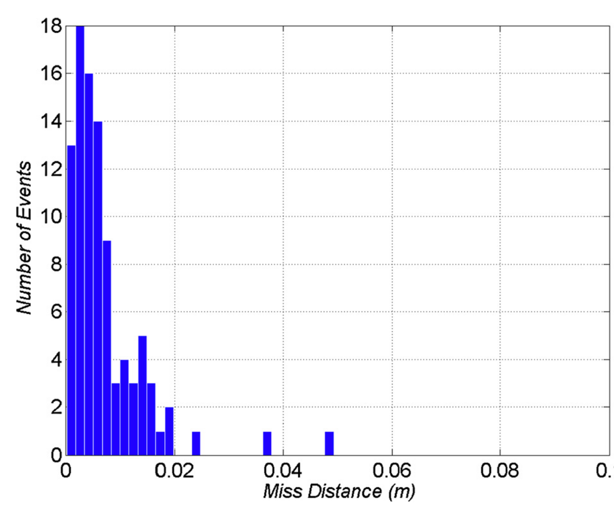

Fig. 19. Nonlinear system simulation – Monte Carlo miss distance.

A batch of 100 Monte Carlo flights were simulated and the point-of-closest-approach was tabulated. Overall, 94% of the projectiles flew within 0.1 m of the moving target. A histogram of the flights within 0.1 m of the target is provided in Fig. 19. Implementing the theoretical models outlined above in simulation with the

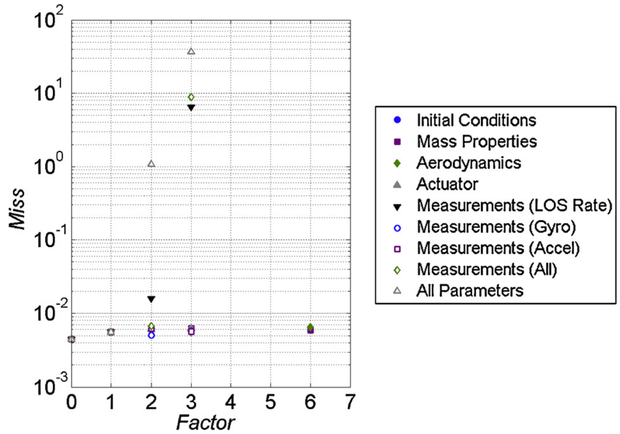

Fig. 20. Nonlinear system simulation – Monte Carlo miss distance trades.

current characteristics for this GNC system yields miss distances often less than 0.02 m.

Monte Carlo trials were performed in the nonlinear system simulation to quantify the relationship between guided performance and system uncertainties. Again, the parameter distributions outlined above were used in the simulations. All uncertainties were scaled by a factor to illustrate trends. Monte Carlo simulations were conducted by isolating each parameter category (e.g., initial conditions, mass properties) and also running all parameter errors together.

These results are provided in Fig. 20. Comparing the initial condition only cases with the all parameter error cases suggests little contribution from initial condition variations. Miss distance will be influenced by initial conditions if the combination of targeting and fire control are so poor that the projectile cannot physically intercept the target.

Mass properties and aerodynamics uncertainties do not greatly contribute to the overall miss distance. Indeed Monte Carlo cases were able to be run with 6 times the nominal error budget for these categories without appreciable changes in the miss distance. Intolerance of the miss distance to these parameters is due to the nature of the feedback control strategy and the magnitude of round-to-round physical (mass and aerodynamics) variability.

Miss distance is also not driven by the actuator characteristics and variability for this system. Miss distances for the actuator only cases are relatively small compared to the all parameter cases. Additionally, miss distance does not vary significantly even when the nominal actuator variability is scaled by a factor of 3.

Measurement errors are the main contributor to miss distance. Monte Carlo miss distances for the measurement only and more specifically the line-of-sight rate errors are similar in magnitude to the all parameter cases. These results suggest proper measurement design (e.g., sensors, electronics) is critical to guided system performance.

6. Conclusions

This paper hypothesized that projectiles can be guided using low cost technologies by accommodating poor sensor and actuators with algorithms and performing high fidelity multidisciplinary modeling and simulation with realistic input data. The nonlinear equations of motion for projectile flight and aerodynamic modeling were presented. Actuator dynamic modeling was performed. Nonlinear measurement models were discussed. Flight model states were manipulated to simulate the response of accelerometers, gyroscopes, and imagers necessary for guidance and flight control. Manipulation of these nonlinear models into linear system models were undertaken for airframe characterization and control design. A framework for guidance and flight control was built. This paper developed a suite of high fidelity model-based flight controllers. Algorithms were designed specifically to facilitate low performance hardware such as actuators with significant time delays (Smith predictor). Practical system characteristics were provided to conduct realistic multidisciplinary simulation and identify cost-performance drivers.

The theory and guidance and flight control strategy was implemented in simulation to illustrate essential features of low cost, high maneuverability GNC systems. Results supported the hypothesis by showing that controlled performance can be drastically improved by designing algorithms which explicitly consider low cost components. Monte Carlo analysis of multidisciplinary modeling and simulations suggested that measurement errors drive guided performance.

Conflict of interest statement

None declared.

References

[1] A. Arrow, D.E. Williams, Comparison of classical and modern missile autopilot techniques, J. Guid. Control Dyn. 12 (2) (1989) 220–227.
[2] B. Davis, G. Malejko, R. Dorhn, S. Owens, T. Harkins, G. Bischer, Addressing the challenges of a thruster-based precision guided mortar munition with the use of embedded telemetry instrumentation, ITEA J. 30 (2009) 117–125.
[3] B. Etkin, Dynamics of Atmospheric Flight, John Wiley & Sons, 1972.
[4] G.F. Franklin, J.D. Powell, A. Emami-Naeini, Feedback Control of Dynamic Systems, Prentice-Hall, 2006.
[5] F.E. Fresconi, Guidance and control of a projectile with reduced sensor and actuator requirements, J. Guid. Control Dyn. 34 (6) (2011) 1757–1766.
[6] F.E. Fresconi, G.R. Cooper, I. Celmins, J. DeSpirito, M. Costello, Flight mechanics of a novel guided spin-stabilized projectile concept, J. Aerosp. Eng. 226 (2011) 327–340.
[7] D.T. Greenwood, Principles of Dynamics, Prentice-Hall, Inc., Englewood Cliffs, NJ, 1965.
[8] N.D. Grubb, M.W. Belcher, Excalibur: new precision engagement asset in the warfight, Fires (Oct.–Dec. 2008) 14–15.
[9] S. Kang, H.J. Kim, J. Lee, B. Jun, M. Tahk, Roll-pitch-yaw, Integrated robust autopilot design for a high angle-of-attack missile, J. Guid. Control Dyn. 32 (5) (2009) 1622–1628.
[10] R.L. McCoy, Modern Exterior Ballistics, Schiffer Publishing Ltd., Atlen, PA, 1999.
[11] J.S. Moorhead, Precision Guidance Kits (PGKs): improving the accuracy of conventional cannon rounds, Field Artillery (Jan.–Feb. 2007) 31–33.
[12] P.H. Morrison, D.S. Amberntson, Guidance and control of a cannon-launched guided projectile, J. Spacecr. Rockets 14 (6) (1977) 328–334.
[13] C.H. Murphy, Free flight motion of symmetric missiles, Report 1216, U.S. Army Ballistics Research Laboratory, Aberdeen Proving Ground, MD, July 1963.
[14] F.W. Nesline, P. Zarchan, Why modern controllers can go unstable in practice, J. Guid. Control Dyn. 7 (4) (1984) 495–500.
[15] F.W. Nesline, B.H. Wells, P. Zarchan, Combined optimal/classic approach to robust missile autopilot design, J. Guid. Control Dyn. 4 (3) (1981) 316–322.
[16] J. Nicolaides, On missile flight dynamics, Ph.D. dissertation, Catholic University of America, 1963.
[17] O.J.M. Smith, A controller to overcome dead time, ISA J. 6 (1959) 28–33.
[18] S.E. Talole, A.A. Godbole, J.P. Kohle, S.B. Phadke, Robust roll autopilot design for tactical missiles, J. Guid. Control Dyn. 34 (1) (2011) 107–117.
[19] D.E. Williams, B. Friedland, A.N. Madiwale, Modern control theory for design of autopilots for bank-to-turn missiles, J. Guid. Control Dyn. 10 (4) (1987) 378–386.
[20] K.A. Wise, D.J. Broy, Agile missile dynamics and control, J. Guid. Control Dyn. 21 (3) (1998) 441–449.
[21] P. Zarchan, Tactical and Strategic Missile Guidance, 5th edition, American Institute of Aeronautics and Astronautics, Reston, VA, 2007.